mater.scichina.com link.springer.com

Published online 29 May 2020 | https://doi.org/10.1007/s40843-020-1348-y
Sci China Mater 2021, 64(1): 96–104

Edge-enriched MoS_2@C/rGO film as self-standing anodes for high-capacity and long-life lithium-ion batteries

Ling Chen[1,2], Yu Liu[3], Zongnan Deng[2], Hao Jiang[1,2*] and Chunzhong Li[1,2]

ABSTRACT **Restraining the aggregation and polysulfide dissolution of edge-enriched metal sulfides is of significance for their applications as anode materials of lithium-ion batteries (LIBs) with high capacity and long cycle-life. In this work, we have reported the incorporation of MoS_2 nanocrystals into amorphous carbon on the surface of reduced graphene oxide (rGO) by balancing the decomposition rates of phenolic resin (PF)-impregnated ammonium thiomolybdate (ATM), which subsequently forms the MoS_2@C/rGO film through redispersion and vacuum filtration. Such structural design effectively avoids the aggregation of MoS_2 nanocrystals and Li_2S loss, and meanwhile ion enrichment in amorphous carbon and diffusion reinforcement can greatly accelerate the electrochemical reaction kinetics. When applied as the self-standing anode, the MoS_2@C/rGO film possesses high reversible capacities of 1164 mA h g^{-1} at the current density of 0.2 A g^{-1} and 810 mA h g^{-1} at 6.4 A g^{-1}. It also exhibits quite a high capacity retention after 1000 cycles at 3.2 A g^{-1}. This work develops the formation theory of incorporation structures and promotes their applications in energy storage devices.**

Keywords: MoS_2 nanocrystals, reduced graphene oxide, edges, lithium-ion batteries, self-standing electrode

INTRODUCTION

Developing novel lithium-ion battery (LIB) anodes with high capacity as well as long cycle life has been a research hotspot motivated by consumer electronics miniaturization in this era [1–4]. As an emerging group of materials, two-dimensional (2D) transition metal sulfides (TMDs) give appealing potential as LIB anodes due to their unique physicochemical properties including abundant active sites, large interlayer space, and countless edge positions, thus exhibiting high pseudocapacitance as well as fast reaction kinetics [5–10]. Especially for molybdenum disulfide (MoS_2), it has the interface space of 0.62 nm to achieve fast charge transportation with the theoretical capacity of 670 mA h g^{-1}, which is considered as a promising alternative for the commercial graphite anode (372 mA h g^{-1}) [11–13]. However, its high ion diffusion barrier, serious structure change, and polysulfide dissolution during the electrochemical process severely limit the improvement of lithium storage capability [14–16].

It has been demonstrated that single/few-layered MoS_2 nanocrystals can accelerate Li^+ diffusion by reducing the energy barrier and mitigate the structural stress caused by volume change based on the results of the first-order reaction dynamics, which is highly favorable to lithiation/delithiation process within charge/discharge cycles [17,18]. Unfortunately, the MoS_2 nanosheets with high surface energy and van der Waals force among sheets easily stack/restack into bulk materials, giving rise to serious capacity fading due to the decreased active sites. Aimed at this issue, coupling single/few-layered MoS_2 nanosheets with carbonaceous substrate is regarded as an effective and applicable strategy [19–21]. For instance, it is reported that the vertical MoS_2 nanosheets can be grown on the surface of electrochemically exfoliated graphene sheets, in which the architecture combines the

[1] Key Laboratory for Ultrafine Materials of Ministry of Education, School of Chemical Engineering, East China University of Science and Technology, Shanghai 200237, China
[2] Shanghai Engineering Research Center of Hierarchical Nanomaterials, School of Materials Science and Engineering, East China University of Science and Technology, Shanghai 200237, China
[3] School of Chemical Engineering and Technology, Sun Yat-sen University, Guangzhou 510275, China
* Corresponding author (email: jianghao@ecust.edu.cn)

advantages of aligned structure and 2D geometry to enhance the lithium storage [13]. Nonetheless, the limited adhesion force between MoS_2 and the substrate always causes partial nanosheet aggregation and structural deterioration, which still remains a grand challenge for LIB application.

To address the mentioned problem, herein, the incorporation of MoS_2 nanocrystals into amorphous carbon is realized on the surface of reduced graphene oxide (rGO) as a high-performance LIB anode. The formation process has been simulated through a thermodynamic and kinetic model, which indicates that balancing decomposition rates of phenolic resin (PF)-impregnated ammonium thiomolybdate (ATM) is the core factor of this structure evolution. Such an intriguing structure with strong adhesion force among MoS_2, amorphous carbon as well as rGO is capable of avoiding nanocrystal aggregation and polysulfide dissolution, and meanwhile accelerating the reaction kinetics by speeding up ion/electron transportation during the charge/discharge process. When applied as the LIB anode, the resulting film can be directly used as a self-standing electrode without any functional agents. Consequently, the MoS_2@C/rGO sample can deliver a high reversible capacity of 1164 mA h g^{-1} at the current density of 0.2 A g^{-1}, and also exhibit ultrafast charge/discharge capability (810 mA h g^{-1} at 6.4 A g^{-1}) as well as superior cycling stability (910 mA h g^{-1} at 3.2 A g^{-1} after 1000 cycles with 84% capacity retention).

EXPERIMENTAL SECTION

Synthesis of the MoS_2@C/rGO film

Typically, 30 mg of GO was firstly added in 20 mL of deionized (DI) water, and then 0.6 g of $(NH_4)_2MoS_4$ (ATM) was added to form solution A. Subsequently, 0.247 g of resorcinol was dissolved in 0.94 g of methanol, and 1 mL of 1.2 mg mL^{-1} Na_2CO_3 solution was then slowly added to form solution B. The solution B was added in solution A dropwise with the viscosity of the solution gradually getting stickier. The mixed solution was transferred to a 50-mL Teflon-lined stainless steel autoclave after being stirred for 30 min and then kept at a controlled temperature of 85°C for 72 h. The grey precipitates were collected by centrifugal separation and freeze-drying. To get a self-standing film, the products (25 mg) were dispersed in the DI water (50 mL) and the film was formed by vacuum filtration. Finally, the as-prepared product was calcined at 700°C for 2 h under Ar atmosphere to obtain the MoS_2@C/rGO self-standing film.

Synthesis of the MoS_2/rGO film

A 150 mg of cetyltrimethylammonium bromide (CTAB) was dissolved in 30 mL of DI water, and then 30 mg of GO was added. After 24 h of stirring under 45°C, 150 mg of $(NH_4)_2MoS_4$ was added with further stirring for 2 h. After hydrothermal reaction, the following procedure was the same as the MoS_2@C/rGO for forming MoS_2/rGO film with the same weight for better comparison.

Characterizations

The surface and cross-sectional morphologies of MoS_2@C/rGO and MoS_2/rGO films were measured by scanning electron microscopy (SEM; Hitachi, S-4800, Japan; 15 kV). Transmission electron microscopy (TEM) images were obtained by a transmission electron microscope (JEOL, JEM-2100F, Japan). The *in-situ* TEM observation was performed using a scanning tunneling microscope-TEM holder (Nanofactory Instruments AB, Sweden) within the JEM-2100F under an operation potential of 200 kV. The microstructures of products were characterized by powder X-ray diffraction (XRD; Rigaku D/Max2550 V, Japan; Cu Kα radiation). A Thermo Scientific EscaLab 250Xi and a Via+ Reflex Raman spectrometer (USA) with the excitation wavelength of 514 nm recorded the X-ray photoelectron spectroscopy (XPS) spectra and Raman spectra, respectively. Electro-spin resonance spectrometer analysis was performed by a Bruker Daltonics EMX-8/2.7 (100G-18KG, Germany). The N_2 adsorption/desorption measurements were carried out by the Micromeritcs ASAP 2010 analyzer and the Brunauer-Emmett-Teller (BET) surface area (S_{BET}) was analyzed by BET theory. Thermogravimetric (TG) analysis was determined by a NETZSCH STA409PC analyzer (Germany) at a rate of 10 °C min^{-1} from room temperature to 700°C. About 8 mg of sample was used in each test.

Electrochemical measurements

The electrochemical measurements were carried out by using the as-prepared films as the working electrode, the pure lithium foil as the counter electrode and the polypropylene membrane (Celgard 2400) as the separator. The coin cells (2016-type) were assembled in the argon-filled glove box with both H_2O and O_2 <0.01 ppm. The electrolyte was a solution of 1 mol L^{-1} $LiPF_6$ in ethylene carbonate (EC)/dimethyl carbonate (DMC) (1:1, *v*/*v*). The charge and discharge measurements were carried out on a LAND-CT2001C test system at different current densities

between 0.01 and 3.0 V *versus* Li/Li^+. Cyclic voltammogram profiles and electrochemical impedance spectra (EIS) tests were performed on an Autolab PGSTAT302N electrochemical workstation.

RESULTS AND DISCUSSION

Fig. 1a illustrated the lithiation/delithiation processes of the MoS_2@C/rGO and the MoS_2/rGO. Notably, no obvious aggregation of MoS_2 nanocrystals can be observed in the MoS_2@C/rGO after delithaton process, while the formation of bulk materials appears in the MoS_2/rGO, indicating the high dispersion of MoS_2 nanosheets can be maintained by incorporating them into amorphous carbon loaded on the rGO surface. In addition, this architecture can also realize pseudocapacitance-dominated Li^+ storage as well as rapid ion/electron transfer during the electrochemical process, thus achieving excellent LIB performance. In order to elucidate the formation of this MoS_2/C incorporated nanostructure, a thermodynamic and kinetic model was deployed to evaluate the homogeneity of MoS_2 and C in the system (the details are provided in Supplementary information). The homogeneity of MoS_2 and C can be denoted as: $R_{MoS_2@C}$, which can be calculated according to the equation below:

$$R_{MoS_2@C} = \frac{C^{(L)}_{MoS_2}(r) / C^{(0)}_{MoS_2}}{C^{(L)}_{C}(r) / C^{(0)}_{C}}, \quad (1)$$

where $C_i^{(L)}(r)$ represents the local concentration of each component i and $C_i^{(0)}$ represents the total concentration of each component i. As shown in Fig. 1b and Fig. S1, the temperatures of 600, 700 and 800°C were applied to calcine the precursors, showing that the curves of $R_{MoS_2@C}$ can reach 1.0 at lower reaction degree at 700 and 800°C than at 600°C, implying high temperature is favorable to improve the homogeneity of MoS_2 and C within the structure. Nonetheless, when the calculation temperature increases to 800°C, the value of $R_{MoS_2@C}$ ascends dramatically with the increase of reaction degree towards 1.0, indicating the decomposition rate of ATM is much faster than the carbonization rate of PF to cause the excessive growth of MoS_2 nanocrystals inside the carbon layers. As a result, the theoretical calculation evidences that 700°C is the optimized temperature to realize MoS_2/C incorporated nanostructure. The conclusion was further verified by the TEM observation. It is clearly visible

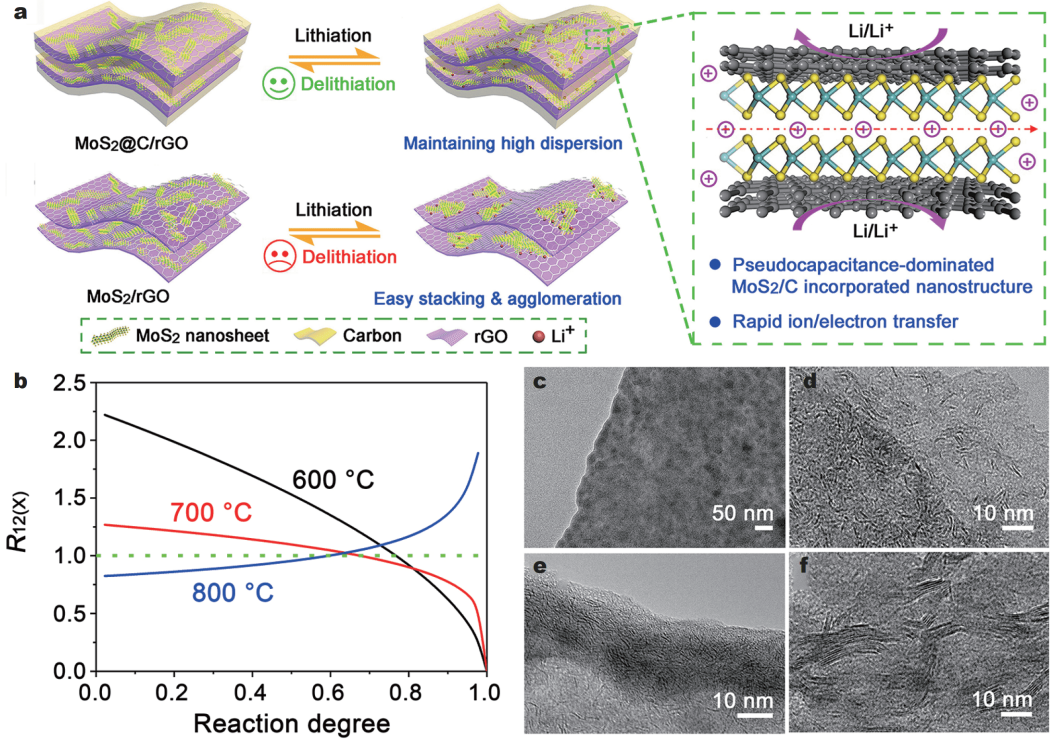

Figure 1 (a) The scheme of lithiation/delithiation processes of the MoS_2@C/rGO and the MoS_2/rGO. (b) Thermodynamic/kinetic prediction of the relative MoS_2 and carbon ratio *versus* reaction degree under different annealing temperatures. (c–f) TEM images of the precursor and the products after annealing at 600, 700, and 800°C.

that the MoS_2 nanocrystals are homogeneously dispersed into the amorphous carbon layers (Fig. 1e) at 700°C (the enlarged TEM image is provided in Fig. S2) in comparison with the corresponding precursors (Fig. 1c), while the samples at 600°C appear with inhomogeneous distribution of the nanocrystals caused by low crystallinity (Fig. 1d), and the samples at 800°C show that the MoS_2 nanocrystals break through the amorphous carbon layer to generate partial aggregation (Fig. 1f). Based on the above results, 700°C is recognized as the proper calcination temperature to form the MoS_2/C incorporated nanostructure.

The regulation of MoS_2 content in the MoS_2@C/rGO is an important consideration to enhance the LIB anode performances. There are three samples with the MoS_2 contents of 54%, 73% and 83% fabricated by controlling the amount of ATM (Fig. S3). The calculation process is given in the Supplementary information. From the SEM images in Fig. S4, the three samples give a similar sheet-like morphology, indicating MoS_2 content has a negligible impact on the structure. The corresponding LIB performances are assessed in Fig. S5, showing the sample with MoS_2 content of 73% can deliver the highest specific capacity at both 0.2 and 3.2 A g^{-1}, and show unobvious capacity fading during 50 cycles. Therefore, the 73% sample is regarded as the optimal one to perform the further investigation. Fig. 2a shows the digital photos of the MoS_2@C/rGO film under a bending state, displaying its great flexibility as a self-standing electrode. The conductivities of these samples are compared in Fig. S6, indicating the value of the MoS_2@C/rGO keeps much higher than that of the MoS_2/rGO during the repeated bending tests from 0 to 1000 times. It means MoS_2@C/rGO film possesses a fast and stable ability of electron transportation. From the cross-section SEM image in Fig. 2b, it is visible that the thickness of the MoS_2@C/rGO film is ~50 μm with abundant distribution of a porous structure. An enlarged SEM image (Fig. 2c) further exhibits a typical 2D structure with an average size of 10 μm as well as the thickness of ~15 nm, which is helpful to form the film through vacuum filtration [22]. The microstructure of the MoS_2@C/rGO was deeply characterized by TEM technique. As shown in Fig. 2d, it can be seen that MoS_2 nanocrystals with enriched edges are dispersed uniformly on the surface of rGO, which can expose more active sites for lithium storage. The corresponding selected area electron diffraction (SAED) exhibits obvious diffraction rings indexed to MoS_2 hexagonal structure (inset of Fig. 2d) [23]. To clarify the combination of MoS_2 nanocrystals and amorphous carbon, nitric acid was utilized to etch the MoS_2 component. TEM image (Fig. 2e) after acid etching shows remained porous distribution throughout the entire layer, indicating the nanocrystals were closely embedded into the amorphous carbon to generate the incorporated structure. This can be also evidenced by BET measurement, as shown in Fig. 2f. The specific surface area of the MoS_2@C/rGO sample gives a sharp change from 37 to

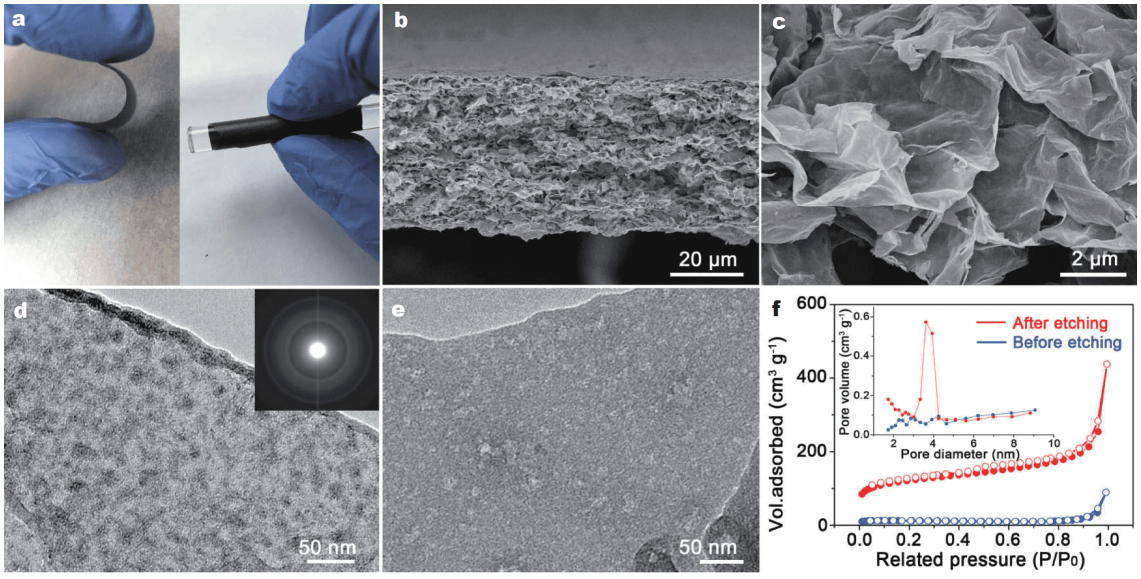

Figure 2 (a) Digital photos, (b, c) cross-section SEM images and (d) TEM image of the MoS_2@C/rGO self-standing film (inset of (d) shows the corresponding SAED pattern). (e) TEM image of the MoS_2@C/rGO after acid etching. (f) N_2 adsorption/desorption isotherms and the pore-size distribution curves of the MoS_2@C/rGO before and after acid etching.

397 $m^2 g^{-1}$ with the appearance of mesoporous structure (~3.7 nm) after acid etching, confirming the incorporation of MoS_2 into the carbon layer.

The structural properties of MoS_2@C/rGO were further characterized by XRD, Raman spectroscopy and XPS with MoS_2/rGO as a reference. The XRD patterns (Fig. 3a) of MoS_2@C/rGO show three characteristic peaks at 14.2°, 33.1° and 58.5° corresponding to (002), (100) and (110) planes of 2H-MoS_2 (JCPDS: 37-1492) [24]. Noteworthily, the carbon characteristic peak at 26.6° (remarked by #, JCPDS: 26-1076) disappears in the MoS_2@C/rGO, and the corresponding peak intensity of (002) plane is much weaker than that of the MoS_2/rGO, also supporting the uniform dispersion of MoS_2 into carbon layer [25]. This is in accordance with the results of the Raman spectra for the MoS_2@C/rGO (Fig. 3b), which show no signals relative to in-plane Mo–S phonon mode (E1 2g) and out-of-plane Mo–S phonon mode (A_{1g}) of MoS_2 [26]. In addition, from the XPS spectra of S 2p (Fig. 3c) and Mo 3d (Fig. S7) of the two samples, the Mo 3d and S 2p peaks for the MoS_2@C/rGO shift to lower binding energies than the MoS_2/rGO, indicating more S-vacancies in the MoS_2@C/rGO hybrids [27]. This is also verified by electron paramagnetic resonance (EPR) measurement (Fig. 3d), displaying the MoS_2@C/rGO has a stronger signal response at ~3500 G than MoS_2/rGO. It indicates that there are more dangling bonds caused by S-vacancies in this sample. The formation of S-vacancies can also enrich active sites to improve LIB performances [28].

To evaluate the electrochemical performances of the MoS_2@C/rGO as anode materials, a half coin-type LIB was assembled with the MoS_2/rGO as a control. Fig. 4a shows the initial three cyclic voltammograms (CV) curves of the MoS_2@C/rGO at 0.2 mV s^{-1} between 0.01 and 3.0 V. The first cathodic scan shows a small peak at 1.1 V, corresponding to the insertion of Li^+ in MoS_2 nanosheets to form Li_xMoS_2. The strong peak at 0.45 V is related to the superposition of the SEI film formation as well as step-by-step conversion to Mo and Li_2S. In the subsequent discharge processes, the cathodic peaks shifted to 1.78 and 1.05 V, implying lithiation reactions occur as shown below: $2Li^+ + S + 2e^- \rightarrow Li_2S$ and $MoS_2 + xLi^+ + xe^- \rightarrow Li_xMoS_2$. In the anodic scan, the peak located at 1.65 V can be assigned to the oxidation of Mo^{4+} to Mo^{6+} and the peak at 2.40 V is assigned to the delithiation of Li_2S. Moreover, the following CV curves for the second and third scans are nearly overlapped, revealing the high electrochemical reversibility of the MoS_2@C/rGO sample [29,30]. The first discharge and charge capacities are 1523 and 1175 mA h g^{-1} with the Coulombic efficiency (CE) of ~77% (Fig. S8). For the second and third cycles, the CE is increased to 96% with a high reversible capacity of

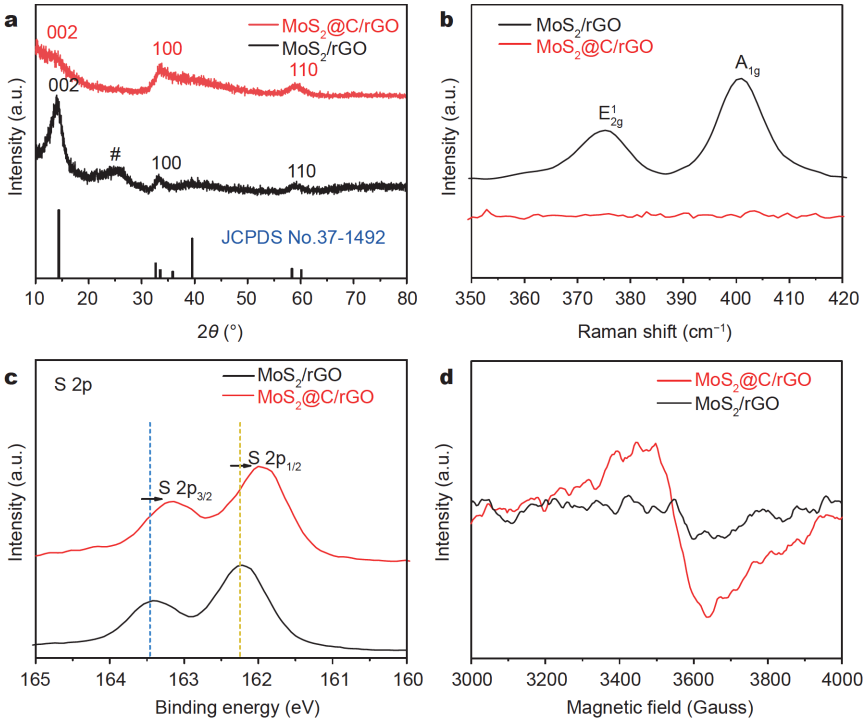

Figure 3 (a) XRD patterns, (b) Raman spectra, (c) S 2p XPS and (d) EPR spectra of the MoS_2@C/rGO and MoS_2/rGO.

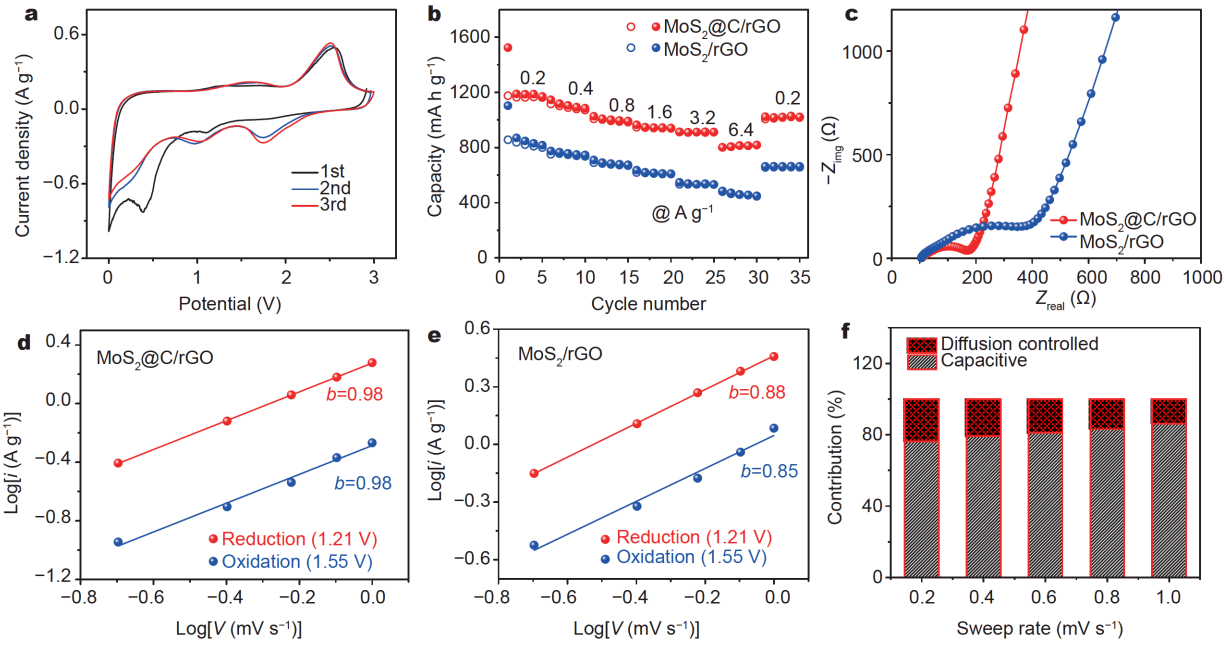

Figure 4 (a) The initial three CV curves at 0.2 mV s^{-1} of the MoS_2@C/rGO film. (b) Rate capabilities and (c) EIS curves of the MoS_2@C/rGO and MoS_2/rGO films. (d, e) log*i* *vs.* log*v* plots of the MoS_2@C/rGO and MoS_2/rGO. (f) Normalized contribution ratio of capacitive and diffusion-controlled capacities of the MoS_2@C/rGO at different sweep rates.

1164 mA h g^{-1}, and the relatvie plateaus are in accordance with the specifc peaks in CV profiles. The rate performance in Fig. 4b shows the MoS_2@C/rGO sample can deliver 1164, 1091, 995, 941, 910 and 810 mA h g^{-1} at the current densities of 0.2, 0.4, 0.8, 1.6, 3.2 and 6.4 A g^{-1}, respectively, and when the current density returns to 0.2 A g^{-1}, the capacity can still recover to 1014 mA h g^{-1}, which are much higher than that of the MoS_2/rGO. The assessment of the reaction kinetics was investigated by EIS measurement. As shown in Fig. 4c, the charge transfer resistance (R_{ct}) of the MoS_2@C/rGO is ~190 Ω, much smaller than that of the MoS_2/rGO (~514 Ω), implying a fast charge transportation at the electrode/electrolyte interface. Meanwhile, a larger slope of the linear trend for the MoS_2@C/rGO is clearly visible compared with the MoS_2/rGO, also indicating a faster Li^+ diffusion during the bulk transportation to achieve a rapid charge/discharge capability. For deeply analyzing the electrode kinetics, CV measurements at various scan rates (0.2–1.0 mV s^{-1}) were performed (Fig. S9) to build the relationship of the sweep rate (v) and peak current (i) based on the equation below:

$$i = av^b, \tag{2}$$

where i is the current response at a certain potential, v is the sweep rate, a and b are adjustable coefficients. It is reported that b=0.5 represents the electrochemical reaction is dominated by the diffusion-controlled mechanism, while b=1 represents a typical non-Faradaic capacitive behavior [31,32]. Fig. 4d, e show the corresponding log*i* *vs.* log*v* plots, where the b values of the MoS_2@C/rGO are 0.98 and 0.98 for the reduction and oxidation processes, superior to those of the MoS_2/rGO (0.88, 0.85), implying a rapid kinetics dominated by a typical capacitive behavior. Furthermore, the contribution ratio of capacitive and diffusion controlled capacities for the MoS_2@C/rGO was calculated according to the following equation:

$$i = k_1v + k_2v^{1/2}, \tag{3}$$

where k_1, k_2 represents the coefficient factor for capacitive and diffusion-controlled processes, respectively. As shown in Fig. 4f, the capacitive contributions are 76.3%, 79.2%, 81.0%, 83.1% and 86.2% with the increasing sweep rate from 0.2 to 1.0 mV s^{-1}, which is in line with the mentioned results. Besides, Fig. S10 shows a voltage profile for the capacitive current (grid region) in comparison with the total current at a sweep rate of 1 mV s^{-1}, which is an analogy to the behavior of metal chalcogenides [33].

Cycling performance is also an indispensable indicator to evaluate electrode materials. Fig. 5a is the comparison of 200-cycle capacity retentions at 0.2 A g^{-1} for the mentioned two samples, giving the value of 97% for the MoS_2@C/rGO, much higher than that for the MoS_2/rGO

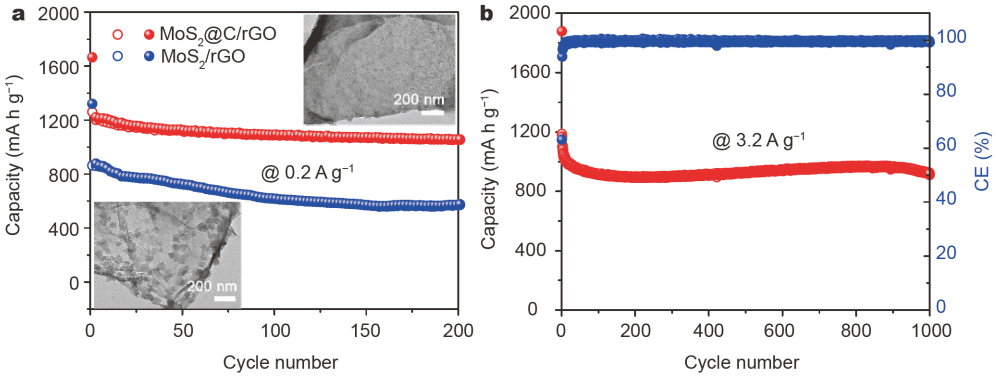

Figure 5 (a) The capacity retention after 200 cycles at 0.2 A g^{-1} for the MoS_2@C/rGO and MoS_2/rGO (insets show the corresponding TEM images). (b) The cycling stability of the MoS_2@C/rGO at 3.2 A g^{-1} for 1000 cycles.

(87%). The corresponding morphology at the potential of 3.0 V *vs.* Li/Li^+ (Li^+ entirely extracted) after the cycling test was characterized by TEM, presenting the integrity of the MoS_2@C/rGO was well-maintained; instead, severe aggregation of the nanocrystals occurred in the MoS_2/rGO. Therefore, it is verified that the amorphous layer is vital to protect the entire architecture to ensure relatively high capacity retention during the electrochemical process. A higher current density of 3.2 A g^{-1} was further deployed to assess the fast charge/discharge cycling capability. As shown in Fig. 5b, the MoS_2@C/rGO anode is capable of steadily cycling over 1000 times without distinct capacity fading. Both the CE at 0.2 and 3.2 A g^{-1} for the MoS_2@C/rGO can quickly increase to 100% after several cycles (Fig. S11). Such outstanding performance is a direct cause of the structural coalition of the MoS_2 nanocrystals, amorphous carbon, and rGO sheet.

To gain deep insight into the structural advantages of the MoS_2@C/rGO, *in-situ* TEM observation was carried out to probe the microstructure evolution during Li^+ lithiation/delithiation. Fig. 6a is the schematic diagram of the *in-situ* TEM configuration, where the MoS_2@C/rGO film attached to a Cu probe as an anode, the Li metal attached to the Au probe as the cathode, and Li metal exposed in the air to form Li_2O layer as the electrolyte. During the testing process, the anode was first moved to contact the electrolyte/cathode (Li/Li_2O) interface by precise piezo-driven manipulation of the TEM-STM holder system, and then a bias of −3.0 V was applied to trigger the Li^+ insertion reaction. A TEM image of the pristine MoS_2@C/rGO sample before the electrochemical process is provided in Fig. 6b, in which the tiled MoS_2@C (marked by green circles in Fig. 6) and the pure MoS_2 nanosheets (marked by yellow circles in Fig. 6) can be distinctively observed. The different stages of Li^+ insertion were recorded in terms of reaction time (1, 5, 10 19, 30 min), as shown in Fig. 6c–g. Surprisingly, there is no visible change of the size and shape for the sample in the green circles, yet, a severe structural deformation can be seen for the sample in the yellow circles. Subsequently, a bias of 3.0 V was performed to start the Li^+ extraction reaction for the MoS_2@C/rGO. Fig. 6h is the corresponding TEM image after 10-times charge/discharge cycles, still showing no sensible structure failures. The *in-situ* TEM observation confirms that the incorporated architecture of the MoS_2@C/rGO is of great essence for keeping the structure integrity when Li^+ lithiation/delithiation gradually proceeds to attain superior rate capability and cycling stablity as LIB anode.

CONCLUSIONS

In summary, the MoS_2@C/rGO self-standing film has been developed as a novel LIB anode, in which MoS_2 nanocrystals are well-incorporated into amorphous carbon loaded on the surface of rGO. Such an impressive structure gives superior lithium storage capability, delivering a high reversible capacity of 1164 mA h g^{-1} at the current density of 0.2 A g^{-1}. More importantly, the resulting film can give 810 mA h g^{-1} even at 6.4 A g^{-1} and 910 mA h g^{-1} at 3.2 A g^{-1} after 1000 cycles, implying the ultrafast charge/discharge capability and great cycling stability. The outstanding electrochemical performances are mainly attributed to the synergistic effect of MoS_2 nanocrystals, amorphous carbon and rGO caused by strong adhesion force inside the entire structure, which can not only avoid the aggregation of the nanocrystals and the dissolution of polysulfides, but also accelerate the reaction kinetics during the charge/discharge process. This can be directly verified by the *in-situ* TEM observation. This work verified the formation of a novel

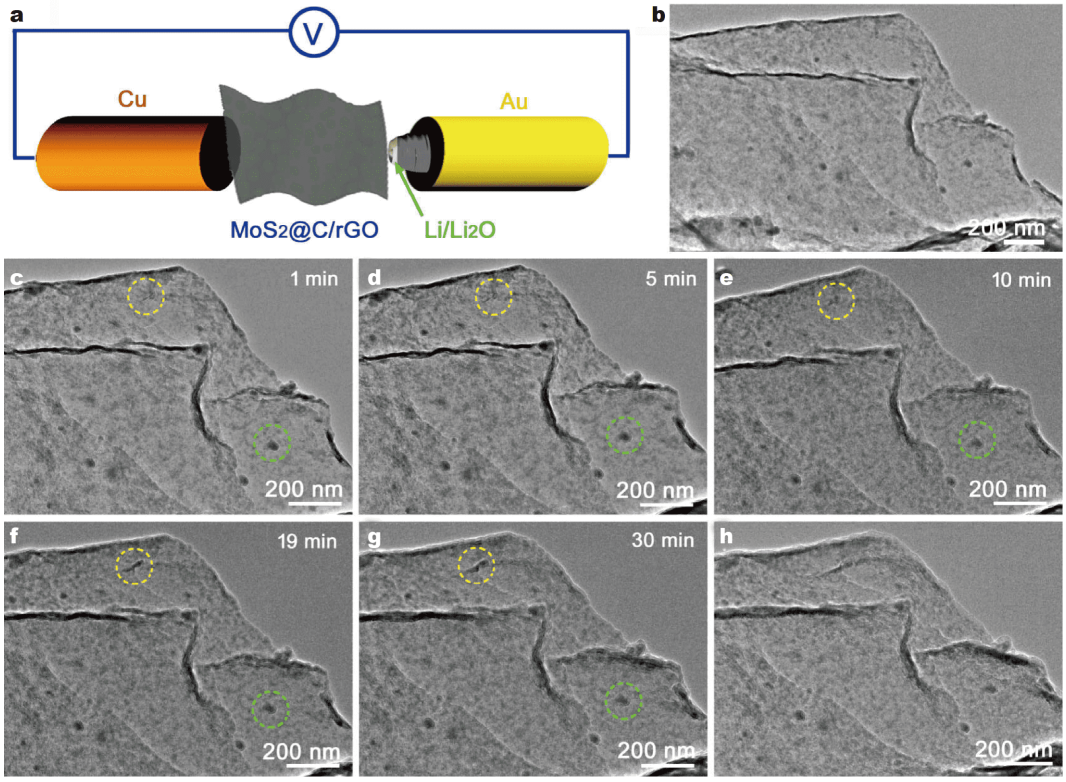

Figure 6 (a) Schematic illustration of the *in-situ* TEM experiment. (b–g) The *in-situ* TEM images of the MoS_2@C/rGO during the lithiation process. (h) TEM image after delithiation for the MoS_2@C/rGO.

incorporation structure, which can guide the design of other advanced LIB anode materials.

Received 12 March 2020; accepted 11 April 2020; published online 29 May 2020

1 Liu J, Bao Z, Cui Y, *et al.* Pathways for practical high-energy long-cycling lithium metal batteries. Nat Energy, 2019, 4: 180–186
2 Yang H, Wu H, Ge M, *et al.* Simultaneously dual modification of Ni-rich layered oxide cathode for high-energy lithium-ion batteries. Adv Funct Mater, 2019, 29: 1808825
3 Huang W, Zhang X, Zheng S, *et al.* Calix[6]quinone as high-performance cathode for lithium-ion battery. Sci China Mater, 2020, 63: 339–346
4 Lin J, Xu Y, Wang J, *et al.* Preinserted Li metal porous carbon nanotubes with high Coulombic efficiency for lithium-ion battery anodes. Chem Eng J, 2019, 373: 78–85
5 Cha E, Patel MD, Park J, *et al.* 2D MoS_2 as an efficient protective layer for lithium metal anodes in high-performance Li–S batteries. Nat Nanotech, 2018, 13: 337–344
6 He H, Huang D, Gan Q, *et al.* Anion vacancies regulating endows MoSSe with fast and stable potassium ion storage. ACS Nano, 2019, 13: 11843–11852
7 Wu C, Ou JZ, He F, *et al.* Three-dimensional MoS_2/carbon sandwiched architecture for boosted lithium storage capability. Nano Energy, 2019, 65: 104061
8 Liu Y, Yu XY, Fang Y, *et al.* Confining SnS_2 ultrathin nanosheets in hollow carbon nanostructures for efficient capacitive sodium storage. Joule, 2018, 2: 725–735
9 Chao D, Zhu C, Yang P, *et al.* Array of nanosheets render ultrafast and high-capacity Na-ion storage by tunable pseudocapacitance. Nat Commun, 2016, 7: 12122
10 Sarwar S, Nautiyal A, Cook J, *et al.* Facile microwave approach towards high performance MoS_2/graphene nanocomposite for hydrogen evolution reaction. Sci China Mater, 2020, 63: 62–74
11 Jiang H, Ren D, Wang H, *et al.* 2D monolayer MoS_2-carbon interoverlapped superstructure: engineering ideal atomic interface for lithium ion storage. Adv Mater, 2015, 27: 3687–3695
12 Yun Q, Lu Q, Zhang X, *et al.* Three-dimensional architectures constructed from transition-metal dichalcogenide nanomaterials for electrochemical energy storage and conversion. Angew Chem Int Ed, 2018, 57: 626–646
13 Wang G, Zhang J, Yang S, *et al.* Vertically aligned MoS_2 nanosheets patterned on electrochemically exfoliated graphene for high-performance lithium and sodium storage. Adv Energy Mater, 2018, 8: 1702254
14 Chen C, Xie X, Anasori B, *et al.* MoS_2-on-MXene heterostructures as highly reversible anode materials for lithium-ion batteries. Angew Chem Int Ed, 2018, 57: 1846–1850
15 Hu X, Li Y, Zeng G, *et al.* Three-dimensional network architecture with hybrid nanocarbon composites supporting few-layer MoS_2 for lithium and sodium storage. ACS Nano, 2018, 12: 1592–1602
16 George C, Morris AJ, Modarres MH, *et al.* Structural evolution of

electrochemically lithiated MoS_2 nanosheets and the role of carbon additive in Li-ion batteries. Chem Mater, 2016, 28: 7304–7310
17 Wu W, Wang L, Li Y, *et al.* Piezoelectricity of single-atomic-layer MoS_2 for energy conversion and piezotronics. Nature, 2014, 514: 470–474
18 Zhu C, Mu X, van Aken PA, *et al.* Single-layered ultrasmall nanoplates of MoS_2 embedded in carbon nanofibers with excellent electrochemical performance for lithium and sodium storage. Angew Chem Int Ed, 2014, 53: 2152–2156
19 You Y, Ye Y, Wei M, *et al.* Three-dimensional MoS_2/rGO foams as efficient sulfur hosts for high-performance lithium-sulfur batteries. Chem Eng J, 2019, 355: 671–678
20 Chen L, Jiang H, Hu Y, *et al. In-situ* growth of ultrathin MoS_2 nanosheets on sponge-like carbon nanospheres for lithium-ion batteries. Sci China Mater, 2018, 61: 1049–1056
21 Sun D, Ye D, Liu P, *et al.* MoS_2/graphene nanosheets from commercial bulky MoS_2 and graphite as anode materials for high rate sodium-ion batteries. Adv Energy Mater, 2018, 8: 1702383
22 Geng X, Jiao Y, Han Y, *et al.* Freestanding metallic 1T MoS_2 with dual ion diffusion paths as high rate anode for sodium-ion batteries. Adv Funct Mater, 2017, 27: 1702998
23 Chen X, Wang Z, Wei Y, *et al.* High phase-purity 1T-MoS_2 ultrathin nanosheets by a spatially confined template. Angew Chem Int Ed, 2019, 58: 17621–17624
24 Wang G, Bi X, Yue H, *et al.* Sacrificial template synthesis of hollow C@MoS_2@PPy nanocomposites as anodes for enhanced sodium storage performance. Nano Energy, 2019, 60: 362–370
25 Zhang S, Wang J, Torad NL, *et al.* Rational design of nanoporous MoS_2/VS_2 heteroarchitecture for ultrahigh performance ammonia sensors. Small, 2020, 16: 1901718
26 Zhou H, Lv P, Lu X, *et al.* Fibrous network of C@MoS_2 nanocapsule-decorated cotton linters interconnected by bacterial cellulose for lithium- and sodium-ion batteries. ChemSusChem, 2019, 12: 5075–5080
27 Xu Y, Wang L, Liu X, *et al.* Monolayer MoS_2 with S vacancies from interlayer spacing expanded counterparts for highly efficient electrochemical hydrogen production. J Mater Chem A, 2016, 4: 16524–16530
28 Li L, Qin Z, Ries L, *et al.* Role of sulfur vacancies and undercoordinated Mo regions in MoS_2 nanosheets toward the evolution of hydrogen. ACS Nano, 2019, 13: 6824–6834
29 Teng Y, Zhao H, Zhang Z, *et al.* MoS_2 nanosheets vertically grown on graphene sheets for lithium-ion battery anodes. ACS Nano, 2016, 10: 8526–8535
30 Chen YM, Yu XY, Li Z, *et al.* Hierarchical MoS_2 tubular structures internally wired by carbon nanotubes as a highly stable anode material for lithium-ion batteries. Sci Adv, 2016, 2: e1600021
31 Zhou L, Zhang K, Sheng J, *et al.* Structural and chemical synergistic effect of CoS nanoparticles and porous carbon nanorods for high-performance sodium storage. Nano Energy, 2017, 35: 281–289
32 Lou P, Cui Z, Jia Z, *et al.* Monodispersed carbon-coated cubic NiP_2 nanoparticles anchored on carbon nanotubes as ultra-long-life anodes for reversible lithium storage. ACS Nano, 2017, 11: 3705–3715
33 Ma K, Jiang H, Hu Y, *et al.* 2D nanospace confined synthesis of pseudocapacitance-dominated MoS_2-in-Ti_3C_2 superstructure for ultrafast and stable Li/Na-ion batteries. Adv Funct Mater, 2018, 28: 1804306

Acknowledgements This work was supported by the National Natural Science Foundation of China (21975074 and 21838003), the Basic Research Program of Shanghai (17JC1402300), Shanghai Scientific and Technological Innovation Project (18JC1410500), and the Fundamental Research Funds for the Central Universities (222201718002).

Author contributions Chen L, Jiang H and Li C conceived the idea and data analysis. Chen L performed the experiments. Liu Y performed the calculation. Deng Z helped to discuss partial experimental data. Chen L and Jiang H wrote the paper. All authors contributed to the general discussion.

Conflict of interest The authors declare that they have no conflict of interest.

Supplementary information Experimental details and supporting data are available in the online version of the paper.

Ling Chen is currently a PhD candidate in materials and science engineering under the supervision of Prof. Hao Jiang at the East China University of Science and Technology. Her research focuses on developing transition metal oxides/dichalcogenides for energy storage and conversion.

Hao Jiang received his PhD degree in materials and science engineering from East China University of Science and Technology (ECUST) in 2009. He then joined Temasek Laboratories, Nanyang Technological University (NTU) in Singapore, as a research scientist from 2009 to 2011. Now, he is a professor in the Key Laboratory for Ultrafine Materials of Ministry of Education at ECUST. His research focuses on the design and synthesis of novel hierarchical nanomaterials for energy storage and conversion.

高比电容量和长寿命的丰富边位MoS_2@C/rGO自支撑膜锂离子电池负极

陈灵[1,2], 刘宇[3], 邓宗南[2], 江浩[1,2*], 李春忠[1,2]

摘要 制备具有丰富边位的金属硫化物纳米晶对于提高其储锂比电容量和延长其循环寿命具有重要意义. 我们通过控制酚醛树脂(PF)碳化速率以及硫代钼酸铵(ATM)分解速率之间的匹配关系, 在还原石墨烯(rGO)表面成功组装了硫化钼(MoS_2)纳米晶嵌入无定形碳复合材料, 随后通过再分散和真空抽滤得到了MoS_2@C/rGO自支撑膜. 这种结构设计有效地避免了电化学反应过程中MoS_2纳米晶的聚集和Li_2S的流失. 同时, 无定形碳层促进了离子富集以及扩散加强, 加快了电化学反应动力学. 当MoS_2@C/rGO自支撑膜作为锂离子负极时, 在0.2和6.4 A g^{-1}的电流密度下分别表现出1164和810 mA h g^{-1}的可逆比电容量. 在3.2 A g^{-1}的电流密度下经过1000次循环仍具有相当高的容量保持率. 该工作为嵌入式结构材料的构筑提供了理论指导, 并促进了其在储能器件中的应用.

